A Self-Rotary Aerial Robot With Passive Compliant Variable-Pitch Wings

Xinyu Cai, Luke Soe Thura Win, Brian Leonard Suhadi, *Graduate Student Member, IEEE*, Hitesh Bhardwaj, and Shaohui Foong, *Member, IEEE*

***Abstract*—Inspired by maple seeds, the self-rotary winged aerial robots reflect the advantages of both multi-rotor aircraft and fixed-wing robots. However, their self-rotating speed is related to the take-off weight, which may affect their application and flight stabilization. To provide a practical and feasible solution, this work proposes a passive compliant variable-pitch mechanism on the self-rotary winged aircraft without requiring extra actuators. Depending on the weight of the payload, the pitching angle of the wings can be passively varied to minimize the increase in the rotating speed and enhance attitude stabilization ability. Besides, an adaptive attitude controller is also designed to address the challenges in attitude stabilization, which are caused by parameter uncertainties and the variable pitching angle. To elaborate on the design and fabrication of the prototype, necessary identification experiments are arranged to find the relationship of pitching angle, thrust generation, power draw, and rotating speed. The experimental findings indicate the proposed robot with optimal pitch angles achieves around 56.8% more power loading than using propellers directly, from 4.4 to 6.9 g/w. The combination of the passive compliant mechanism and adaptive controller improves flight performance from 0.16 to 0.08 meters (mean of absolute translational error).**

***Index Terms*—Underactuated robots, aerial systems: mechanics, control and applications.**

I. Introduction

UNMANNED aerial vehicles (UAVs), such as quadcopters, are believed to have great potential in many fields thanks to their maneuverability when interacting with the environment [1]. However, this ability of a single vehicle is limited by the maximal thrust it can produce, which is mainly related to its physical design, such as the size and number of rotors. In recent years, to address this challenge and be capable of heavier payloads, many approaches and strategies have been studied by researchers, such as the development of modular and reconfigurable airframes [2], [3], optimal thrust configuration [4], [5], cooperative tasking with multiple robots [6], etc.

Unlike conventional multirotors producing lift via propellers directly, the self-rotary winged aerial robot (Fig. 1) seems to be able to generate extra thrust by making use of its huge airfoils [7]. However, the inevitability of self-rotating motion may also limit its implementations and applications. Especially, when the rotating speed goes high, some of the applications would be severely impacted. For example, the dynamic range of a commercialized IMU (inertia measurement unit), which is widely used in onboard flight attitude estimation, is usually limited to around 35 rd/s [8]. Similarly, high rotating speed would also cause unexpected blur to the applications with a camera [7] or Lidar (Light detecting and ranging) system [9]. However, for a self-rotary winged robot, its thrust generation is related to the self-rotating speed. That implies the extra payload requires a faster-rotating speed to hover, resulting in an even higher angular momentum in flight. This causes difficulties in flight attitude control as a higher torque generation is required to overcome the gyroscopic effect [10].

Previous studies related to self-rotating winged aerial robots, such as [7], [11], [12], show great potential in flight efficiency. However, this is achieved by overcoming the severe underactuation and relying on the inherited passive flight attitude [13]. As a consequence, those reported self-rotating winged aerial robots are usually sensitive to the modification of their mass distribution and flight equilibrium. To enhance the control authority, extra

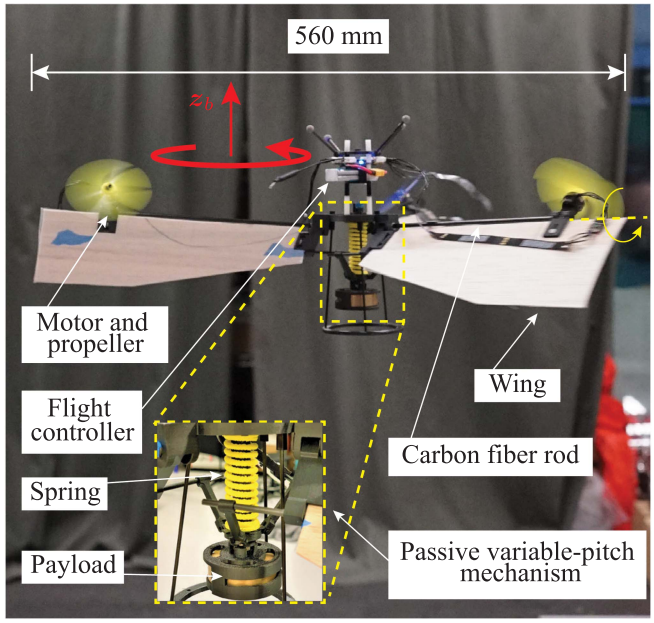

Fig. 1. A self-rotary aerial vehicle with passive compliant variable-pitch wings carrying a payload. The thrusts of the propellers are used for both self-rotation generation and attitude stabilization. And the lifting force is mostly produced by the aerodynamic force from wings.

Manuscript received 7 December 2022; accepted 16 April 2023. Date of publication 29 May 2023; date of current version 6 June 2023. This letter was recommended for publication by Associate Editor M. Bangura and Editor P. Pounds upon evaluation of the reviewers' comments. *(Corresponding author: Shaohui Foong.)*

The authors are with the Engineering Product Development Pillar, Singapore University of Technology and Design (SUTD), Singapore 487372 (e-mail: xinyucai2-c@my.cityu.edu.hk; thura_soe@sutd.edu.sg; brian_suhadi@sutd.edu.sg; hitesh_bhardwaj@mymail.sutd.edu.sg; shao@sutd.edu.sg).

This letter has supplementary downloadable material available at https://doi.org/10.1109/LRA.2023.3280827, provided by the authors.

Digital Object Identifier 10.1109/LRA.2023.3280827

This work is licensed under a Creative Commons Attribution-NonCommercial-NoDerivatives 4.0 License. For more information, see https://creativecommons.org/licenses/by-nc-nd/4.0/

actuators can be added to obtain more degrees of freedom of control, such as [14], [15]. However, this strategy increases both manufacturing costs and controlling complexity. Besides, studies like [8], [16] also show the attempts with event cameras to address the problem caused by fast dynamic rotation, and valuable achievements have been gained.

In this study, we introduce a self-rotary aerial robot with three passive compliant variable-pitch wing (as shown in Fig. 1). By applying the passive mechanism, the proposed robot become less-sensitive to mass modification. The potential payload is connected to the airframe through a passive variable-pitch structure, allowing the pitch angle passively changed with the attached weights. Besides, considering the possible dynamic uncertainties caused by the complex force and torque generation, and the varying pitching angle in our case, an adaptive attitude controller inspired by [17] is proposed by deriving from a Lyapunov candidate containing both the flight attitude error and parameter error.

The main contributions of this letter are listed as follows: 1) a passive variable-pitch mechanism is designed to reduce the changes in rotating speed when an extra payload is attached; 2) an optimized pitching angle of wings is found by detailed system identification; 3) an adaptive attitude controller is developed to handle with the dynamical uncertainties caused by the passive variable-pitch mechanism; 4) actual flight experiments with extra payload are arranged to evaluate the effectiveness of the proposed strategy.

II. System Modelling

A. Force and Torque Modelling

A robotic platform has three symmetrically distributed wings as shown in Fig. 1 and illustrated in Fig. 2(a). Details of the prototype can be found in Section IV-A. In the plane formed by the wing profile, a motor-propeller actuator is perpendicularly mounted to its wing span direction. All three propellers spin in Counter-Clock-Wise (CCW) direction. The body-fixed frame, with $\boldsymbol{x}_b$, $\boldsymbol{y}_b$, $\boldsymbol{z}_b$ denoting its x, y and z axis respectively, is attached to its center of mass (Com). To introduce the forces and torques produced in the body-fixed frame, we use variables θ and ϕ to denote the pitching and rotary angle between wings and the body-fixed frame. That is, θ_i denotes the angle of the ith wing and the plane formed by $\boldsymbol{x}_b$ and $\boldsymbol{y}_b$, ϕ_i denotes the angle of the leading edge of the ith wing and $\boldsymbol{x}_b$, details can be found in Fig. 2(a) and (b). In this study, we limit the consideration to a symmetric configuration, meaning $\theta_i = \theta$, $\phi_1 = 0$, $\phi_2 = \frac{2}{3}\pi$, $\phi_3 = \frac{4}{3}\pi$ (in rads). Hence, the forces and torques produced by the propeller can be calculated in the body-fixed frame, as

$$\begin{bmatrix} f_x \\ f_y \\ f_z \\ \tau_x \\ \tau_y \\ \tau_z \end{bmatrix} = \begin{bmatrix} -\sum f_i \sin\phi_i \cos\theta \\ \sum f_i \cos\phi_i \cos\theta \\ \sum f_i \sin\theta \\ \sum f_i \sin\phi_i l_m \sin\theta + \sum \tau_i \sin\phi_i \cos\theta \\ \sum f_i \cos\phi_i l_m \sin\theta + \sum \tau_i \cos\phi_i \cos\theta \\ -\sum \tau_i \sin\theta + \sum f_i l_m \cos\theta \end{bmatrix} \tag{1}$$

where f_i and τ_i are the thrust and reaction torque generated by the ith propeller, i = 1, 2, 3. l_m denotes the distance between propeller and Com. Unlike other conventional multi-rotor aerial robots, the proposed self-rotary winged aircraft generates fast rotating speed (Ω) about its primary axis to achieve high hovering efficiency. To model the aerodynamic force f_w produced

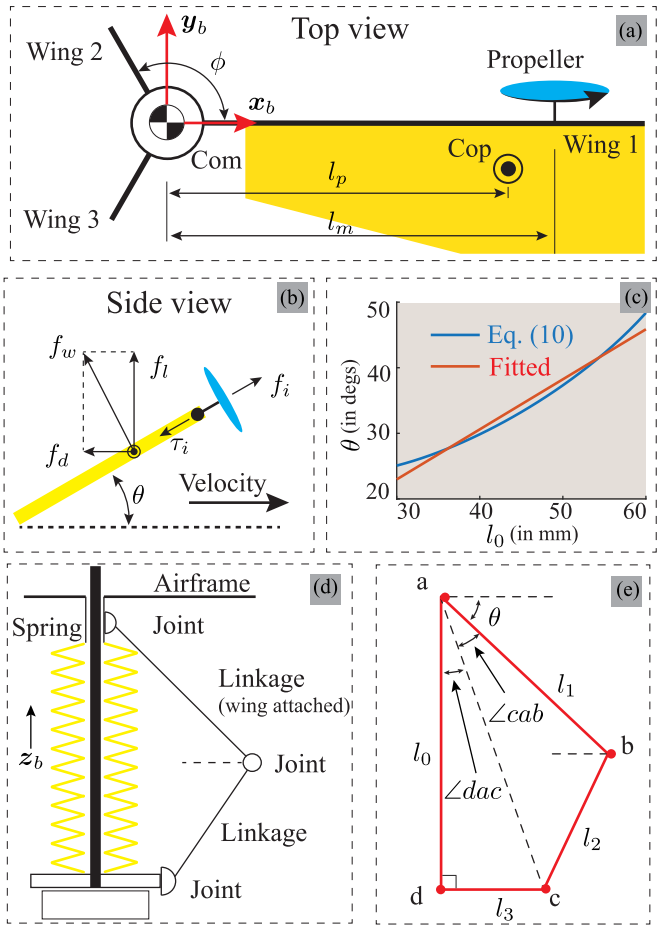

Fig. 2. (a) and (b) show the top and side view respectively. (c) shows the approximation to (10). (d) is an abstracted model of the passive mechanism. (e) illustrates the geometry relationship of the passive mechanism, where $\angle dac$ and $\angle cad$ are calculated by solving triangle $\triangle adc$ and $\triangle cad$ respectively.

by wings, like other rotary winged robots, we simply apply the Blade Element Theory (BET) and approximate the sum of them on an assumed Center of pressure (Cop), as

$$f_{l,d} = \frac{1}{2}\rho C_{l,d}(\alpha) A V^2, \tag{2}$$

where $f_{l,d}$ are lift and drag force, ρ is the air density, $C_{l,d}$ are the lift and drag coefficient respectively. Considering the unsteady aerodynamics due to the revolving motion [18], the model of lift and drag coefficients are approximated by $C_l(\alpha) = C_{l,1}\sin(2\alpha)$, $C_d(\alpha) = C_{d,0} + C_{d,1}(1 - \cos(2\alpha))$ [7], where $C_{l,1}, C_{d,0}, C_{d,1}$ are experimentally determined, α is the angle of attack. A is the wing area, and V is the relative air speed to free air stream. Details can refer to Fig. 2(b). Considering the symmetric configuration and near-hovering flight (when the rotating axis $\boldsymbol{z}_b$ is pointing upward), the aerodynamic force from wings can be regarded as identical. As a result, forces and torques in $\boldsymbol{x}_b$ and $\boldsymbol{y}_b$ are balanced with each other, leaving forces and torques only in $\boldsymbol{z}_b$ axis, formulated as

$$f'_z = f_{l,1} + f_{l,2} + f_{l,3}, \tag{3}$$

$$\tau'_z = -(f_{d,1} + f_{d,2} + f_{d,3}) l_p, \tag{4}$$

where $f_{l,i}$ and $f_{d,i}$ are the ith lift and drag force respectively, l_p is the distance of Cop and Com, shown in Fig. 2(a). For a self-rotating robot, the effect of precession motion also adds some challenges to the force and torque modelling. Compared to propellers and wings, the torque caused by precession motion is minor, and we use $\tau_{x,p}$ and $\tau_{y,p}$ to represent this effect on $\boldsymbol{x}_b$ and $\boldsymbol{y}_b$ axes respectively. Details of the modelling of the precession torque can refer to our previous work [11], [19]. Combining all the effects from propellers, wings, and precession motion, we obtain the full expression of force and torque in the body-fixed frame.

B. Flight Dynamics Modelling

With the analysis and modelling of forces and torque expressed in the body-fixed frame, we can simply introduce the flight dynamics to the proposed robot. Let vector $\boldsymbol{f} = [f_x, f_y, f_z + f_z']^T$, $\boldsymbol{\tau} = [\tau_x + \tau_{x,p}, \tau_y + \tau_{y,p}, \tau_z + \tau_z']^T$ denote the collective force and torque respectively in body frame. Let a 3×3 rotation matrix $\boldsymbol{R} = [\boldsymbol{i}, \boldsymbol{j}, \boldsymbol{k}]$ describe the mapping from body frame to world frame, $\boldsymbol{p} = [p_x, p_y, p_z]^T$ denote the position of the robot in the world frame. Like other rigid bodies, the rotational and translational dynamics can be modeled by applying Euler's equation and Newton's law, as

$$\begin{bmatrix} \boldsymbol{\tau} \\ \boldsymbol{Rf} \end{bmatrix} = \begin{bmatrix} \boldsymbol{I}\dot{\boldsymbol{\omega}} + \boldsymbol{\omega}_{\times}\boldsymbol{I}\boldsymbol{\omega} \\ m\ddot{\boldsymbol{p}} + mg\boldsymbol{e}_3 \end{bmatrix} = \boldsymbol{A}\boldsymbol{u} \tag{5}$$

where $\boldsymbol{I}$ is a 3×3 inertia matrix, $\boldsymbol{\omega} = [\omega_x, \omega_y, \omega_z]^T$ is the angular velocity about principal axes, m is the total mass, g is the gravitational constant, $\boldsymbol{e}_3 = [0, 0, 1]^T$ is a basis vector, $\boldsymbol{A}$ is a 6×3 actuation mapping matrix, which is derived from the torque and force generation equations introduced in previous Section II-A. $\boldsymbol{u} = [f_1, f_2, f_3]^T$ is the actuation vector.

C. Optimization Modelling for Hovering

Due to its own flight character, the proposed robot can hardly meet the restricted hovering condition with both zero translational and angular velocity. Following the concept of 'relaxed hovering' introduced in [20], we can easily find the conditions, as $\boldsymbol{f} = [0, 0, mg]^T$, $\boldsymbol{\tau} = \boldsymbol{0}^{3\times1}$. This necessitates, $f_i = \bar{f}$, $f_{l,d,i} = \bar{f}_{l,d}$. Combined with (5), the relaxed hovering conditions can be simplified as

$$\bar{f} l_m \cos\theta - \bar{f} c_o \sin\theta - \bar{f}_d l_p = 0, \tag{6}$$

$$\bar{f}\sin\theta + \bar{f}_l = \frac{1}{3}mg, \tag{7}$$

where c_o is the coefficient to denote the ratio of torque to thrust of a propeller, as $c_o = \frac{\tau}{f}$. Combining (2), (6) and (7), we obtain

$$\bar{f}\left(\sin\theta + \frac{C_l}{C_d}\frac{l_m\cos\theta - c_o\sin\theta}{l_p}\right) = \frac{1}{3}mg. \tag{8}$$

To achieve optimal flight efficiency, we aim to find a suitable pitching angle θ to minimize the mean thrust ($\bar{f}$) from propellers, as

$$\theta^* = \max_{\theta}(\sin\theta + \frac{C_l}{C_d}\frac{l_m\cos\theta - c_o\sin\theta}{l_p}). \tag{9}$$

Equation (9) implies that the optimal pitching angle θ^* is related to the C_l, C_d, l_m, c_o and l_p, which are decided by combination effects including the geometry of wing profile, position of motor, propellers, and the pitching angle. To simplify the consideration, we leave only the pitching angle as a variable and regard other parameters as constant values. In this way, we are able to identify the optimal pitching angle θ^* by arranging practical tests, which will be introduced in future Section IV.

D. Passive Compliant Variable-Pitch Mechanism Modelling

To achieve the ability to passively increase the pitching angle θ when the weight of the payload goes heavier, we introduce the passive compliant variable-pitch structure including a linear extension spring, free joints and rigid linkages, illustrated by Fig. 2(d). The top side of the spring is connected to the airframe, and the bottom side is connected to the payload adapter. A free sliding rod inside the spring and the airframe guarantee the spring stretches along $\boldsymbol{z}_b$. In this way, the passive variable-pitch structure can be abstracted to a simple quadrilateral, denoted by S_{abcd} in Fig. 2(e). Note that the wing is attached with linkage $\bar{ab}$, meaning its angular deviation from the horizontal is the pitching angle θ. To model the relationship of angle θ and the length of the spring, we use l_0, l_1, l_2, and l_3 to denote the length of each side of the quadrilateral introduced in Fig. 2(e). Note that l_0 is a variable denoting the spring length while other sides are constant, and the angle between $\bar{ad}$ and $\bar{dc}$ is perpendicular. Using the existing geometric relationships, we obtain

$$\begin{aligned}\theta &= \frac{\pi}{2} - \angle dac - \angle cab \\ &= \frac{\pi}{2} - \arctan\frac{l_3}{l_0} - \arccos\frac{l_0^2 + l_1^2 + l_3^2 - l_2^2}{2l_1\sqrt{l_0^2 + l_3^2}}.\end{aligned} \tag{10}$$

To simplify the consideration and provide more insights, we approximate the relationship described by (10) with a linear function ($\theta = k_0 l_0 + b_0$) by using the parameters of our prototype (introduced in Section IV), $l_1 = 40$ mm, $l_2 = 30$ mm, $l_3 = 15$ mm. Details are shown in Fig. 2(c), where $l_0 \in [30, 60]$ mm, $k_0 = 0.763$, $b_0 = 0.084$. According to Hooke's law, the spring length can be represented as $l_0 = \bar{l}_0 + \frac{f}{k_1}$, where $\bar{l}_0$ is the relaxed length of spring, f is the stretching force, k_1 is the spring constant. Considering a payload with mass M is attached to the robot, then the pitching angle θ can be re-written as

$$\theta = \frac{k_0}{k_1}Mg + k_0\bar{l}_0 + b_0. \tag{11}$$

So far, we obtain the relationship between the payload mass (M) and the pitching angle θ.

III. Flight Controller

A. Near-Hovering Assumptions

In order to overcome the underactuation and develop a practical flight controller (as shown in Fig. 3), in this section, we introduce the following assumptions under the near-hovering equilibrium:

1) We assume the forces produced in $\boldsymbol{x}_b$ and $\boldsymbol{y}_b$ are small, as $f_x \approx 0$, $f_y \approx 0$. In this way, we can decouple the rotational and translational dynamics and apply the cascaded controlling structure [21].
2) We assume the rotating velocity is nearly constant in the flight. In this way, the collective lifting force generated by wings is independent of the controlling inputs. In other words, altitude dynamics is only related to the spinning

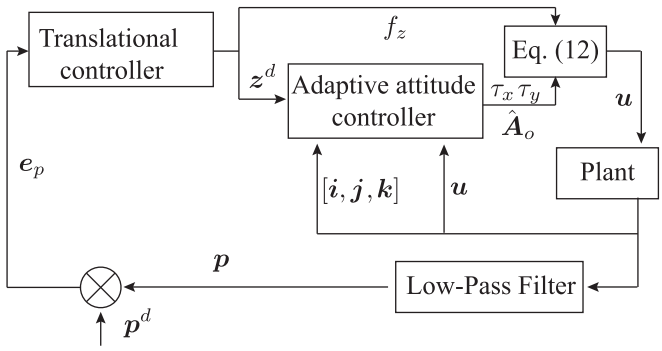

Fig. 3. The proposed flight controller with a cascaded structure.

speed of propellers, which allows us to consider altitude dynamics as a second-order equation and apply a standard proportional-integral-derivative (known as PID) controller to address the height error.

Note the rotating motion (the angular deviation about z axis) is not a controlling goal of the attitude controller, then the flight dynamics shown by (5) can be reduced as

$$\begin{bmatrix}\tau_x\\ \tau_y\\ f_z\end{bmatrix} = \begin{bmatrix} I_x\dot{\omega}_x + W_x\\ I_y\dot{\omega}_y + W_y\\ m\ddot{p}_z - f_z' + mg\end{bmatrix} = \boldsymbol{A}_o\boldsymbol{u}, \tag{12}$$

where $I_{x,y}$ is the moment of inertia about $\boldsymbol{x}_b$ and $\boldsymbol{y}_b$ respectively, $W_{x,y}$ is the first and second row of term $\boldsymbol{\omega}_\times\boldsymbol{I}\boldsymbol{\omega}$ respectively. $\boldsymbol{A}_o$ is a 3×3 matrix, obtained from (1). Like other cascaded control structures, the horizontal translational controller is realized by stabilizing a proper flight attitude with respect to the world frame.

B. Adaptive Attitude Controller

The aim of the attitude controller is to stabilize the flight attitude, which is denoted by its rotating axis $\boldsymbol{z}_b$ in our case. Let a 3×1 unit vector $\boldsymbol{z}^d$ represent the desired rotating axis. Then, the attitude error in $\boldsymbol{x}_b$ and $\boldsymbol{y}_b$ axis can be calculated by

$$e_x = \boldsymbol{j}^T\cdot\boldsymbol{z}^d, \quad e_y = -\boldsymbol{i}^T\cdot\boldsymbol{z}^d, \tag{13}$$

where $\boldsymbol{i}$ and $\boldsymbol{j}$ are the first and second column of rotating matrix $\boldsymbol{R}$, meaning the representation of $\boldsymbol{x}_b$ and $\boldsymbol{y}_b$ with respect to world frame, respectively. In practice, the variable-pitching mechanism (introduced in Fig. 1, Fig. 2(d) and described in Section II-D) and the difficulties of obtaining accurate modelling of the precession motion may introduce possible parameter uncertainties to the mapping matrix $\boldsymbol{A}_o$. Different from our previous work [19], we consider a Lyapunov function L consists both attitude error $\boldsymbol{e} = [e_x, e_y]^T$ and the uncertainties of the mapping matrix $\tilde{\boldsymbol{A}}_o$. Let $\boldsymbol{A}_{o,xy}$ denote the first two rows of matrix $\boldsymbol{A}_o$, let $\hat{\boldsymbol{A}}_{o,xy}$ and $\tilde{\boldsymbol{A}}_{o,xy}$ denote the estimation and error of $\boldsymbol{A}_{o,xy}$, yielded by $\tilde{\boldsymbol{A}}_{o,xy} = \boldsymbol{A}_{o,xy} - \hat{\boldsymbol{A}}_{o,xy}$. Let $\boldsymbol{\alpha} = [\alpha_{11}, \alpha_{12}, \alpha_{13}, \alpha_{21}, \alpha_{22}, \alpha_{23}]^T$ denote the collection of all the elements of matrix $\boldsymbol{A}_{o,xy}$, $\hat{\boldsymbol{\alpha}}$ denote the estimation of $\boldsymbol{\alpha}$, similarly, $\tilde{\boldsymbol{\alpha}} = \boldsymbol{\alpha} - \hat{\boldsymbol{\alpha}}$. Let vector $\boldsymbol{s} = \boldsymbol{\kappa}[e_x, e_y]^T + [\omega_x, \omega_y]^T$, where $\boldsymbol{\kappa} = \mathrm{diag}(\kappa_x, \kappa_y)$. Finally, the Lyapunov candidate is proposed as

$$L = \frac{1}{2}\boldsymbol{s}^T\boldsymbol{s} + \frac{1}{2}\tilde{\boldsymbol{\alpha}}^T\boldsymbol{\Gamma}\tilde{\boldsymbol{\alpha}}, \tag{14}$$

where $\boldsymbol{\Gamma} = \mathrm{diag}(\gamma_1, \gamma_2, \gamma_3, \gamma_4, \gamma_5, \gamma_6)$, denotes the adaptive gain for each element of $\boldsymbol{\alpha}$. Taking the time derivative of L, we obtain

$$\dot{L} = \boldsymbol{s}^T\dot{\boldsymbol{s}} + \tilde{\boldsymbol{\alpha}}^T\boldsymbol{\Gamma}\dot{\tilde{\boldsymbol{\alpha}}}, \tag{15}$$

where $\dot{\boldsymbol{s}} = \boldsymbol{\kappa}[\omega_x, \omega_y]^T + [\dot{\omega}_x, \dot{\omega}_y]^T$. Combining with (12), we have

$$\begin{bmatrix}\dot{\omega}_x\\ \dot{\omega}_y\end{bmatrix} = \boldsymbol{I}_{xy}^{-1}\left\{\begin{bmatrix}\tau_x\\ \tau_y\end{bmatrix} - \begin{bmatrix}W_x\\ W_y\end{bmatrix}\right\} \tag{16}$$

$$= \boldsymbol{I}_{xy}^{-1}\left\{\boldsymbol{A}_{o,xy}\boldsymbol{u} - \begin{bmatrix}W_x\\ W_y\end{bmatrix}\right\} \tag{17}$$

$$= \boldsymbol{I}_{xy}^{-1}\left\{(\hat{\boldsymbol{A}}_{o,xy} + \tilde{\boldsymbol{A}}_{o,xy})\boldsymbol{u} - \begin{bmatrix}W_x\\ W_y\end{bmatrix}\right\}, \tag{18}$$

where $\boldsymbol{I}_{xy} = \mathrm{diag}(I_x, I_y)$. Substituting (18) into (19) and rearranging, we obtain

$$\dot{L} = \boldsymbol{s}^T\left\{\boldsymbol{\kappa}\begin{bmatrix}\omega_x\\ \omega_y\end{bmatrix} + \boldsymbol{I}_{xy}^{-1}\hat{\boldsymbol{A}}_{o,xy}\boldsymbol{u} - \boldsymbol{I}_{xy}^{-1}\begin{bmatrix}W_x\\ W_y\end{bmatrix}\right\} + \boldsymbol{s}^T\boldsymbol{I}_{xy}^{-1}\tilde{\boldsymbol{A}}_{o,xy}\boldsymbol{u} + \tilde{\boldsymbol{\alpha}}^T\boldsymbol{\Gamma}\dot{\tilde{\boldsymbol{\alpha}}}. \tag{19}$$

To guarantee $\dot{L}$ is non-positively defined, we derive the control signal $\boldsymbol{u}$ and updating law $\dot{\hat{\boldsymbol{\alpha}}}$ by solving following equations

$$\boldsymbol{s}^T\left\{\boldsymbol{\kappa}\begin{bmatrix}\omega_x\\ \omega_y\end{bmatrix} + \boldsymbol{I}_{xy}^{-1}\hat{\boldsymbol{A}}_{o,xy}\boldsymbol{u} - \boldsymbol{I}_{xy}^{-1}\begin{bmatrix}W_x\\ W_y\end{bmatrix} r\right\} = -\boldsymbol{s}^T\boldsymbol{\kappa}_p\boldsymbol{s}, \tag{20}$$

$$\boldsymbol{s}^T\boldsymbol{I}_{xy}^{-1}\tilde{\boldsymbol{A}}_{o,xy}\boldsymbol{u} + \tilde{\boldsymbol{\alpha}}^T\boldsymbol{\Gamma}\dot{\hat{\boldsymbol{\alpha}}} = 0, \tag{21}$$

where $\boldsymbol{\kappa}_p = \mathrm{diag}(\kappa_x, \kappa_y)$ is the positively defined attitude control gain matrix. Thus, we ensure that $\dot{L} = -\boldsymbol{s}^T\boldsymbol{\kappa}_p\boldsymbol{s} \le 0$ by substituting (20) and (21) into (19). In practical flight, τ_x and τ_y in (12) are calculated with the updated $\boldsymbol{A}_{o,xy}$ and $\boldsymbol{u}$.

The negative defined property of $\dot{L}$ implies that the value of the proposed Lyapunov candidate in (14) will decrease once the attitude error $\boldsymbol{s}$ is non-zero. This means the attitude and estimation errors are reduced until the attitude errors are eliminated. Compared to the use of a traditional PID controller, which modifies the control torque directly by assuming a linearized model, the proposed adaptive controller addresses the attitude error by adapting the actuation matrix $\hat{\boldsymbol{A}}_{o,xy}$. In other words, the proposed adaptive controller is more suitable for the problem caused by the uncertainties of the dynamical model.

C. Translational Controller

Like other conventional multirotors, translational control can be achieved by stabilizing the flight attitude (represent by the rotating axis with respect to the world frame) at the desired angle. We use $\boldsymbol{z}_b \approx [\xi_x, \xi_y, 1]^T$ to present the rotation axis with respect to the world frame, with $|\xi_x|, |\xi_y| \ll 1$. Then, the translational dynamics around near-hovering equilibrium can be simplified as

$$m\begin{bmatrix}\ddot{p}_x\\ \ddot{p}_y\end{bmatrix} = mg\begin{bmatrix}\xi_x\\ \xi_y\end{bmatrix}, \quad m\ddot{p}_z = f_z + f_z' - mg, \tag{22}$$

where f_z is the thrust components generated by propellers along the rotation axis, f_z' is the lifting force produced by the wings, which is considered as a constant value and previously introduced in (3) and (12). This implies that the translational

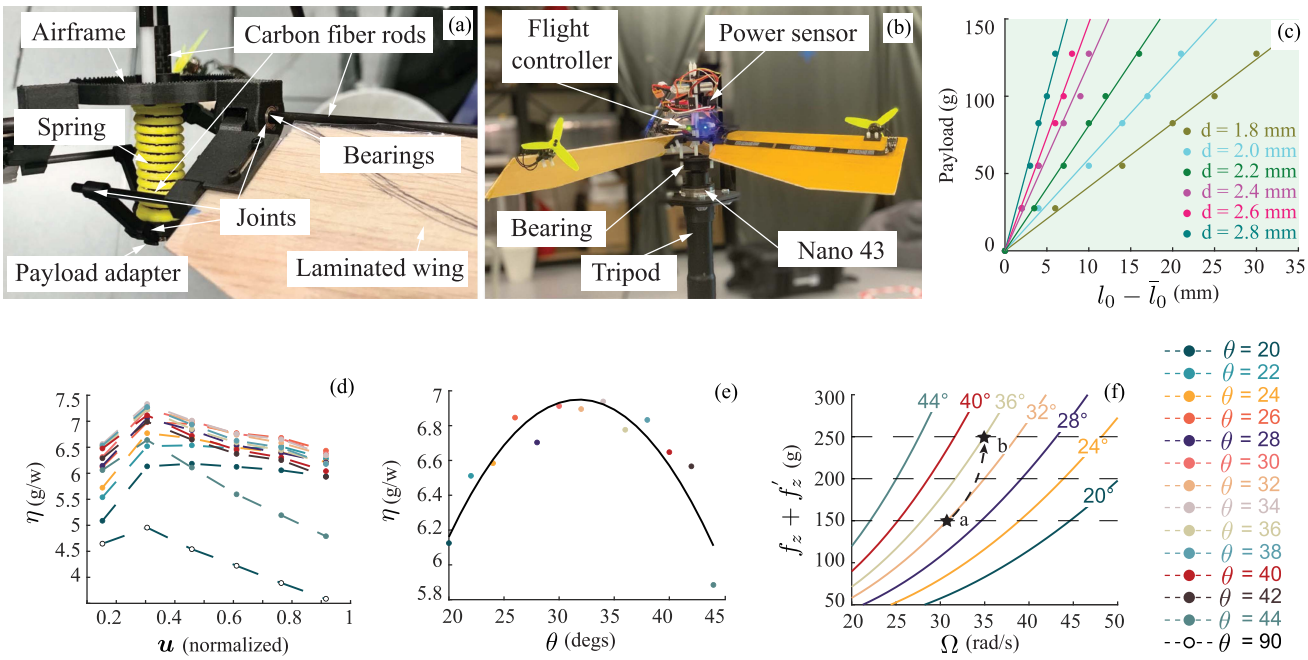

Fig. 4. (a) illustrates the details of the fabrication of the passive variable-pitch mechanism. (b) is the setup of the identification experiment of the optimal pitching angle. (c) is the result of the spring coefficient identification with different diameters of coils. The dots are measurements and the lines are the fitted model. (d) shows the power loading with different controlling inputs for different pitching angles. (e) indicates the optimal pitching angle with respect to power loading. (f) indicates the relationship of rotating speed, collective thrust and pitching angle.

controller can be realized by stabilizing the flight attitude ($\boldsymbol{z}_b$) and the collective thrust of the propellers (f_z).

We use $\boldsymbol{p}^d = [p_x^d, p_y^d, p_z^d]^T$ to present the reference point in the world frame, and the position error is denoted by $\boldsymbol{e}_p = [e_{px}, e_{py}, e_{pz}]^T$. The function of the translational controller is to calculate the desired rotating axis ($\boldsymbol{z}^d = [\xi_x^d, \xi_y^d, 1]^T$) and the desired collective thrust (f_z). To achieve this, we firstly represent the position error e_{px} and e_{py} in a polar coordinates, as

$$\delta = \arctan \frac{e_{py}}{e_{px}}, \quad \epsilon = k_p \sqrt{e_{py}^2 + e_{px}^2}, \tag{23}$$

where k_p is a positive controlling gain, δ is the phase and ϵ is the magnitude. And we have the desired flight attitude, as

$$\xi_x^d = \cos\delta \sin\epsilon, \quad \xi_y^d = \sin\delta \sin\epsilon. \tag{24}$$

Note that $\delta \in (-\pi, \pi]$. For height control, a standard PID controller is employed, formulated by

$$f_z = k_{p,pz} e_{pz} + k_{i,pz} \int e_{pz} dt + k_{d,pz} \dot{e}_{pz}, \tag{25}$$

where $k_{p,pz}$, $k_{i,pz}$, $k_{d,pz}$ are positive controlling gains.

IV. Prototype Fabrication and Identification

A. Prototype Description

The prototype of the reported robot is made up of four primary components: the airframe, wings, flight electronics, and the passive compliant variable-pitch structure. The airframe is a combination of customized 3D-printed parts and three carbon fiber rods with 4-mm diameter to provide rigid connections to actuators and wings. The wings are constructed from a 200-mm, 50-mm, 1-mm balsa sheet, reinforced with plastic lamination. The flight electronics include three brushless DC motors with propellers, a flight control board (Crazyflie Bolt), ESC (electronic speed control), as well as a two-cell Li-Po battery, details can refer to Fig. 1 and Fig. 4(a).

The details of passive compliant variable-pitch structure (shown in Fig. 4(a)), which mainly consists of three constant-length linkages, a customized, 3D-printed linear spring as well as a payload adapter. To provide necessary constraints and rigidity to the prototype, a carbon fiber rod with 10-mm diameter is inserted inside the inner circle of the spring. One end of the carbon fiber is fixed on the payload adapter, and the other end can go through the airframe and freely move up and down. The airframe and payload adaptor is rigidly connected such that the spring can be vertically stretched by the payload.

B. Identification of Optimal Pitching Angle

Noticing the fact it is challenging to obtain the accurate parameters for the analytical expression of the optimal pitching angle (as described in (9)). Thus, in this section, we arrange force testing to find an optimal pitching angle θ^* to minimize the power consumption. In addition, the relationship between the pitching angle (θ), rotating speed (Ω), collective thrust ($f_z + f_z'$) as well as the corresponding power consumption (P). The experimental setup is shown in Fig. 4(b), a prototype with a constant pitching angle is mounted on a tripod via a ball bearing. The wings are placed 1.5 meters away from the ground to avoid the possible ground-effect. The collective thrust generated by the robot is measured by a force sensor (ATI, Nano 43). To measure the power consumption, a circuit with a current sensor (INA-260) is developed and connected together with the flight controller. The rotating speed is calculated from the records of the motion capture system (OptiTrack). The testing range of the pitching

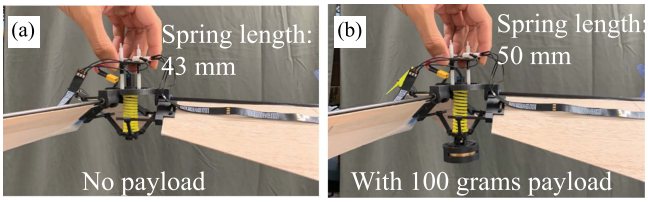

Fig. 5. The prototype of passive compliant structure with selected spring coefficient $k_1 \approx 12$. (a) shows the free spring length ($l_0 \approx 43$ mm) with no payload, and (b) shows the spring length $l_0 \approx 50$ mm when around 100-gram payload is attached. The pitching angle also goes from around 32 to 38 degrees when the payload.

angle is chosen from 20 to 44 degrees with 2 degrees as a step. For reference, we also include the configuration when the wings are vertically installed, $\theta = 90$ degrees. To cover most of the working range of each configuration, the motor command is chosen from around 15% to 90% with 15% as one step. In the testing, each configuration has been repeated 3 times, and their average value is chosen for analysis.

In Fig. 4(d), we plot the relationship between the motor command ($\boldsymbol{u}$) and power loading ($\eta = \frac{f_z + f'_z}{P}$, with the unit of grams per watt, g/w) for all the configurations. Compared to the configuration with vertically installed wings ($\theta = 90$ degrees), the rotating configurations ($\theta \in [20, 44]$ degrees) show significantly higher power efficiency. To find the optimal pitching angle θ^*, we use the average power loading (from 30% to 75% of motor commands) to present the flight efficiency for each configuration. By fitting all the configurations with a second-order polynomial, we have the relationship between the pitching angle and flight efficiency, and we find the optimal pitching angle θ^* is around 32 degrees, shown in Fig. 4(e).

C. Identification and Selection of Passive Compliant Mechanism

With the relationship between thrust producing, rotating speed, and pitching angle (as plotted in Fig. 4(f)), we need to develop the passive compliant variable-pitching mechanism with proper coefficients to match with, which is detailed by (11). Such that, the proposed robot can work with both relatively high power efficiency and small fluctuation in the rotating speed. Using the previously introduced parameters, $l_1 = 40$ mm, $l_2 = 30$ mm, $l_3 = 15$ mm, and the relationship between l_0 and θ, the relaxed length of the spring $\bar{l}_0$ is chosen as 40 mm to allow the robot to work with the optimal pitching angle θ^*. To find a proper coefficient, a set of diameters of the spring coil is fabricated and identified, details as shown in Fig. 4(c).

In our case, the proposed robot weighs about 150 grams, and the extra payload for testing is about 100 grams. When the pitching angle is around 32 degrees, the robot needs to rotate about 30 rd/s to hover, as shown in point "a" in Fig. 4(f). To achieve the goal of maintaining both high flight efficiency and small changes in rotating speed, the passive mechanism is expected to increase around 4–6 degrees of pitching angle when 100 grams payload is attached. As shown by point "b" in Fig. 4(f), the robot needs to rotate only 3 rd/s faster to hover but still obtain relatively high flight efficiency. To achieve that, we choose a spring with $d = 2.4$ mm, $k_1 \approx 12$ in Fig. 4(c). Substituting to (11), we obtain $\theta = 0.06M + 32$. Details of the selected structure can be found in Fig. 5.

V. Experimental Validation

A. Experimental Setup

All the experiments are carried out in an indoor environment equipped with motion capture cameras. The position and attitude measurements from the motion capture system are used for both controlling and ground-truth purposes. The algorithm and calculation are processed in a Python environment in a ground station computer, and the wireless communication between the robot and the ground station is accomplished with Crazyradio PA. More details of the experimental setup can be found in our previous work [11].

B. Adaptive Attitude Stabilization

To show the effects of the adaptive terms in (14), we first arranged the attitude stabilization experiments for the cases with and without payload (around 100 g). Considering the possible drifting with only the attitude controller, the robot takes off and hovers in the middle of the flying area with an altitude of 1.2 meters with the position control in the first 20 seconds. From 20 seconds to 50 seconds, the flight controller switches to attitude control with a constant reference of $\boldsymbol{z}^d = [0, 0, 1]^T$ and the altitude control with a constant height setpoint of 1.2 meters. For the first 15 seconds, the adaptive gain matrix $\boldsymbol{\Gamma}$ is set to be zeros. While for the second 15 seconds, the adaptive terms are enabled. The details of the attitude errors are plotted in Fig. 6(a) and (b). To highlight the contribution of the adaptive terms, we also plot the square of the attitude errors in a log scale in Fig. 6(c). In the flights, the changes of the $\boldsymbol{\alpha}$ are provided in Fig. 6(d) and (i). The results indicate that the adaptive terms can effectively correct the mapping matrix $\boldsymbol{A}_o$ to eliminate the attitude error.

Note that the initial guess of the mapping matrix $\hat{\boldsymbol{A}}_o$, the adaptive gain matrix $\boldsymbol{\Gamma}$, and the attitude control gain $\boldsymbol{\kappa}_p$ are set to be identical for two different cases (with and without payload). Higher fluctuations are observed in blue color owing to the extra payload. Still, the flight attitudes can be reliably stabilized thanks to a higher pitching angle providing more force to attitude control even maintaining a relatively small attitude gain.

C. Hovering Flights

With the purpose of further evaluating the proposed cascaded flight controller and passive variable-pitch mechanism with a payload, we manage three different situations for hovering flights: A, passive variable-pitch mechanism without adaptive terms; B, passive variable-pitch mechanism with adaptive terms; C, fixed pitch angle without adaptive terms. Considering the adaptive attitude controller contains only the errors of flight attitude and mapping matrix, it may cause problems when using it in a controlling loop with position error. In other words, the attitude error calculated from the position error may cause the wrong updating to $\boldsymbol{\alpha}$. To this end, we design a small period of attitude control before putting the position error in the loop. After this, the adaptive gains $\boldsymbol{\Gamma}$ are set to be zeros. Each flight contains an attitude control stage, a take-off stage, a hovering stage, and a landing stage. Each situation has been repeated three times. Both attitude and position errors of the hovering stage are calculated and shown by boxplots in Fig. 7.

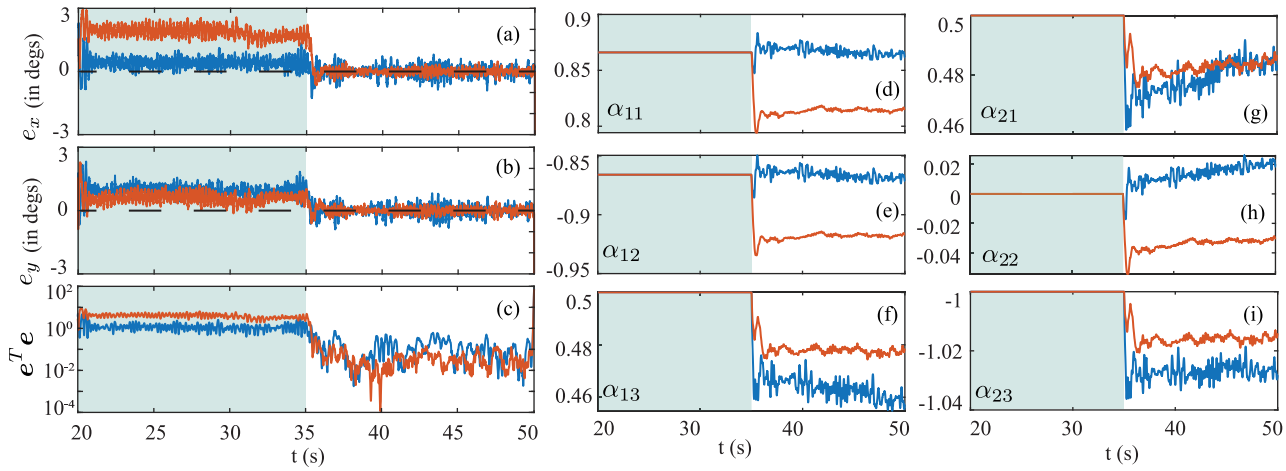

Fig. 6. Plots (a) to (c) are the comparison of the attitude error. Plots (d) to (i) show the comparison of parameter $\boldsymbol{\alpha}$ in the flight. The shadowed portion represents the adaptive terms are disabled, while the blank portion indicates the adaptive terms that are enabled. Blue and red lines are with and without payload respectively.

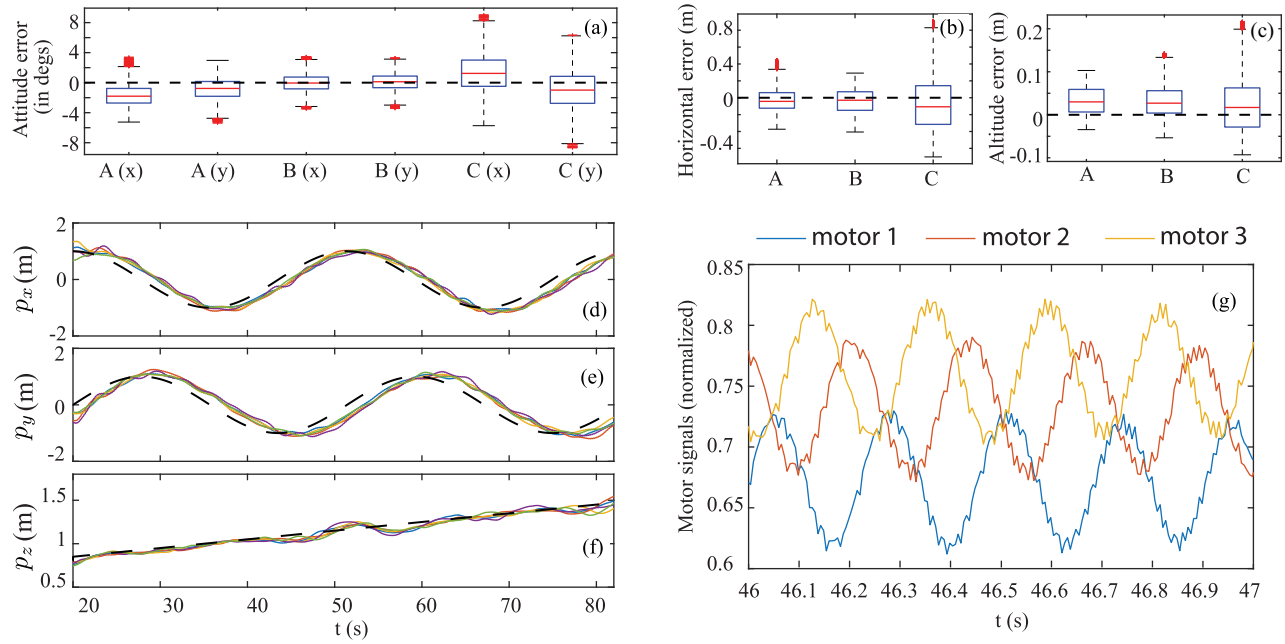

Fig. 7. The top box plots show the comparison of attitude (a) and position errors (b), (c) of different configurations (a), (b), and (c) in hovering flights. All the box plots follow the default setting of the MATLAB (MathWorks) function 'boxplot'. Plots (d), (e), and (f) are the flight trajectories in axis x, y and z respectively when tracking a helix path. Solid lines (5 flights are plotted) are the actual positions, and dashed lines are the reference. The plot of the motors' signal in one flight during 46–47 s is shown in (g).

Note that the controlling gains for all the situations maintain the same for a fair comparison. For the performance of attitude stabilization, the contribution of the passive variable-pitch mechanism and adaptive terms can be validated by comparing case A with case C and B respectively (as shown in Fig. 7(a). In Fig. 7(b) and (c), the improvement in position control is not obvious (by comparing case A with case B) even though the adaptive terms are employed. That is because the main factors affecting position control performance are from the near-hovering assumptions. But the existence of the passive variable mechanism shows visible improvement in position control (by comparing cases A, B with C). As the higher pitching angle can reduce the rotating speed, resulting in a small angular momentum. On the other hand, a higher pitching angle allows higher torque generation to respond the position errors.

Another aspect to validate the contribution of the passive variable-pitch mechanism is the rotation speed for each configuration. When there is no payload attached and the spring is relaxed, the pitching angles of the wings are around 32 degrees. And its rotation speed in hovering is around 26.7 rd/s. With an extra 100-gram payload attached and maintaining the same pitching angle, it requires a higher rotating speed to hover, at around 36 rd/s. By employing the passive variable-pitch mechanism, the rotating speed remains similar to the one without payload, around 28.7 rd/s (compared to 26.7 rd/s). It is necessary to point out that the hovering rotating speeds of

each case show differences to the force identification result (4. F), which is mainly caused by the inaccurate modelling of the passive mechanism and the potential force measurement errors.

D. Trajectory Following

To verify the proposed flight controller and aerial platform in the trajectory following tasks, we design a helix path with a radius of 1 m, the height varies from 0.8 to 1.5 meters, for the situation with both 100-gram payload and passive mechanism. To maintain the near-hovering assumption and minimize the aerodynamic forces caused by horizontal traveling, we limit the tracking velocity to around 0.2 meters per second. The flight has repeated 5 times and the positions with respect to the reference in x, y, and z axis of the world frame are plotted in Fig. 7(d), (e), and (f).

To show the effectiveness of the proposed strategy, a simple comparison of the experimental results has been made. In [11], the root mean square error in horizontal and altitude error of path-tracking are 0.39 and 0.09 meters respectively. In this work, the corresponding values are 0.28 and 0.04. In [19], the root mean square error in horizontal and altitude error of hovering flights are 0.15 and 0.03 meters respectively, while in this work, the corresponding values are 0.12 and 0.04 meters. Note that the proposed robot carries an extra 100-gram payload and uses a set of constant control gains in all flights.

VI. Conclusion

In this work, we have developed a passive compliant variable-pitch mechanism for a three-winged self-rotary aircraft. With the simplified mathematical modeling of the proposed system, we further developed a practical flight controller and prototype. The results of the flight experiment with extra payload indicate that the proposed strategy can effectively reduce the sensitiveness and stabilize the flight attitude of a winged self-rotary robot exposed to mass modification.

References

[1] M. A. Estrada, S. Mintchev, D. L. Christensen, M. R. Cutkosky, and D. Floreano, "Forceful manipulation with micro air vehicles," *Sci. Robot.*, vol. 3, no. 23, 2018, Art. no. eaau6903.

[2] B. Mu and P. Chirarattananon, "Universal flying objects: Modular multi-rotor system for flight of rigid objects," *IEEE Trans. Robot.*, vol. 36, no. 2, pp. 458–471, Apr. 2020.

[3] F. Schiano, P. M. Kornatowski, L. Cencetti, and D. Floreano, "Reconfigurable drone system for transportation of parcels with variable mass and size," *IEEE Robot. Automat. Lett.*, vol. 7, no. 4, pp. 12150–12157, Oct. 2022.

[4] S. Driessens and P. Pounds, "The triangular quadrotor: A more efficient quadrotor configuration," *IEEE Trans. Robot.*, vol. 31, no. 6, pp. 1517–1526, Dec. 2015.

[5] Y. Qin, W. Xu, A. Lee, and F. Zhang, "Gemini: A compact yet efficient bi-copter UAV for indoor applications," *IEEE Robot. Automat. Lett.*, vol. 5, no. 2, pp. 3213–3220, Apr. 2020.

[6] J. Fink, N. Michael, S. Kim, and V. Kumar, "Planning and control for cooperative manipulation and transportation with aerial robots," *Int. J. Robot. Res.*, vol. 30, no. 3, pp. 324–334, 2011.

[7] S. Bai, Q. He, and P. Chirarattananon, "A bioinspired revolving-wing drone with passive attitude stability and efficient hovering flight," *Sci. Robot.*, vol. 7, no. 66, 2022, Art. no. eabg5913.

[8] M. Ng, Z. M. Er, G. S. Soh, and S. Foong, "Aggregation functions for simultaneous attitude and image estimation with event cameras at high angular rates," *IEEE Robot. Automat. Lett.*, vol. 7, no. 2, pp. 4384–4391, Apr. 2022.

[9] C. H. Tan, D. S. B. Shaiful, E. Tang, G. S. Soh, and S. Foong, "Flydar: A passive scanning flying LIDAR sensing system for slam using a single laser," *IEEE Sensors J.*, vol. 22, no. 2, pp. 1746–1755, Jan. 2022.

[10] S. H. Crandall, "The effect of damping on the stability of gyroscopic pendulums," in *Theoretical, Experimental, and Numerical Contributions to the Mechanics of Fluids and Solids*. Berlin, Germany: Springer, 1995, pp. 761–780.

[11] X. Cai, S. K. H. Win, L. S. T. Win, D. Sufiyan, and S. Foong, "Cooperative modular single actuator monocopters capable of controlled passive separation," in *Proc. IEEE Int. Conf. Robot. Automat.*, 2022, pp. 1989–1995.

[12] E. R. Ulrich, D. J. Pines, and J. S. Humbert, "From falling to flying: The path to powered flight of a robotic samara nano air vehicle," *Bioinspiration Biomimetics*, vol. 5, no. 4, 2010, Art. no. 045009.

[13] R. Å. Norberg, "Autorotation, self-stability, and structure of single-winged fruits and seeds (samaras) with comparative remarks on animal flight," *Biol. Rev.*, vol. 48, no. 4, pp. 561–596, 1973.

[14] D. Sufiyan, L. S. T. Win, S. K. H. Win, G. S. Soh, and S. Foong, "Joint mechanical design and flight control optimization of a nature-inspired unmanned aerial vehicle via collaborative co-evolution," *IEEE Robot. Automat. Lett.*, vol. 6, no. 2, pp. 2044–2051, Apr. 2021.

[15] H. Bhardwaj, X. Cai, S. K. H. Win, and S. Foong, "Design, modeling and control of a two flight mode capable single wing rotorcraft with mid-air transition ability," *IEEE Robot. Automat. Lett.*, vol. 7, no. 4, pp. 11720–11727, Oct. 2022.

[16] S. Sun, G. Cioffi, C. De Visser, and D. Scaramuzza, "Autonomous quadrotor flight despite rotor failure with onboard vision sensors: Frames vs. events," *IEEE Robot. Automat. Lett.*, vol. 6, no. 2, pp. 580–587, Apr. 2021.

[17] P. Chirarattananon, K. Y. Ma, and R. J. Wood, "Adaptive control of a millimeter-scale flapping-wing robot," *Bioinspiration Biomimetics*, vol. 9, no. 2, 2014, Art. no. 025004.

[18] W. B. Dickson and M. H. Dickinson, "The effect of advance ratio on the aerodynamics of revolving wings," *J. Exp. Biol.*, vol. 207, no. 24, pp. 4269–4281, 2004.

[19] X. Cai, S. K. H. Win, H. Bhardwaj, and S. Foong, "Modeling, control and implementation of adaptive reconfigurable rotary wings (AROWs)," *IEEE/ASME Trans. Mechatron.*, early access, Jan. 26, 2023, doi: 10.1109/TMECH.2023.3235346.

[20] M. W. Mueller and R. D'Andrea, "Relaxed hover solutions for multicopters: Application to algorithmic redundancy and novel vehicles," *Int. J. Robot. Res.*, vol. 35, no. 8, pp. 873–889, 2016.

[21] D. Mellinger, N. Michael, and V. Kumar, "Trajectory generation and control for precise aggressive maneuvers with quadrotors," *Int. J. Robot. Res.*, vol. 31, no. 5, pp. 664–674, 2012.